INORGANIC CHEMISTRY FRONTIERS

RESEARCH ARTICLE

View Article Online
View Journal | View Issue

Cite this: *Inorg. Chem. Front.*, 2025, **12**, 4334

Enhanced negative permittivity by A-site heterovalent ion doping in $La_{1-x-y}Ca_xK_yMnO_3$ perovskites†

Meichun Fu,[a] Mei Han,[a] Yuan Zhang,[a] Beining Zheng *[b] and Shouhua Feng *[a]

Received 15th December 2024,
Accepted 14th March 2025

DOI: 10.1039/d4qi03217a

rsc.li/frontiers-inorganic

Adjusting the concentration of free carriers is a direct strategy to achieve ideal negative permittivity. Employing chemical methods for atypical ion doping is an effective approach to regulate the concentration of free carriers. Owing to the A-site tunability of perovskite manganese oxides, doping with multivalent ions becomes particularly favorable. In this study, to realize temperature-stable negative permittivity, mono-phase $La_{1-x-y}Ca_xK_yMnO_3$ (named LCKMO) perovskite crystals having diverse compositions were prepared using an ultra-high-alkaline hydrothermal method. Heterovalent ion doping (La^{3+}, Ca^{2+}, and K^+) at the A site within the perovskite crystal structure occurred with the help of the disproportionation reaction of Mn ions at the B site under extreme hydrothermal conditions. By adjusting the La/Ca ratio, we can vary the doping content of K^+. Experimental results demonstrate that as the concentration of K^+ increases, so does the concentration of Mn oxide states, indicating that the increase in free carriers contributes to enhanced negative permittivity and reduced dielectric loss. This work thus pioneers a novel synthetic pathway for the creation and design of materials having negative permittivity.

Introduction

Negative permittivity ($\varepsilon' < 0$), considered a supernormal property and an artificial property, has been previously achieved using periodic arrays.[1] Recently, the study of negative dielectric constant materials has become a prominent area of research.[2,3] Metamaterials and composite materials whose modulation is based on metal building blocks or intrinsic properties and microstructure of materials, respectively, are generally considered typical negative permittivity materials.[4,5] However, owing to the complexity and instability of metamaterials and composite materials, they are difficult to use in practical working conditions, especially under high-temperature or high-acid/-alkaline conditions.[6,7] To overcome this limitation, mono-phase materials have been developed as an alternative using feasible methods, such as band structure modification, defect creation, and vacancy formation, to regulate their negative permittivity.[8]

Perovskites are a typical mono-phase negative dielectric material having a flexible structure that allows optimization of dielectric properties by doping with different cations or component modulation.[9–13] Especially, in the perovskite manganate system, the introduction of A-site dopants alters the Mn^{3+}/Mn^{4+} ratio, thereby inducing changes in physical properties that can be attributed to double exchange (DE) and Jahn–Teller effects.[14–17] For example, the doping of Ca in $LaCaMnO_3$ causes a significant dielectric response in the material.[18] In addition, Sun *et al.* demonstrated that by modulating the concentration of Sr^{2+} in $La_{1-x}Sr_xMnO_3$, a synergistic effect of dielectric resonance and plasma oscillations can be achieved, which results in the simultaneous observation of both Lorentz-like and Drude-like negative permittivity in LSMO ceramics.[19]

Nevertheless, the effect of A-site substitution with divalent ions (Sr, Ca, Ba, and Pb) on the mechanism is primarily attributed to the exchange effect, and the ability to induce free carrier generation is weak.[8,20] Based on the Drude or Lorentz model, free charge carriers are key factors that enhance negative dielectric properties because of their thermal excitation and plasma oscillation.[21] The above regulation of negative dielectric properties is limited to the substitution doping of divalent or trivalent ions at the A site. In terms of changing the states of local and itinerant electrons in a perovskite system, stronger heterovalent doping provides an effective strategy. Compared with the doping of trivalent ions with divalent ions, the doping of monovalent ions induces considerable

[a]*State Key Laboratory of Inorganic Synthesis and Preparative Chemistry, Jilin Provincial International Cooperation Key Laboratory of Advanced Inorganic Solid Functional Materials, College of Chemistry, Jilin University, Changchun, Jilin, 130012, P. R. China. E-mail: shfeng@jlu.edu.cn*
[b]*College of Physics, Jilin University, Changchun 130012, P. R. China. E-mail: zhengbeining@jlu.edu.cn*

†Electronic supplementary information (ESI) available. See DOI: https://doi.org/10.1039/d4qi03217a

fluctuations in the electric potential and considerable charge fluctuations, which is a two-fold strategy to divalent doping.[22,23] However, monovalent ion doping by a high-temperature solid-phase or sol–gel method often leads to issues such as phase separation and oxygen vacancy.[24,25] To avoid the above problems, it is necessary to explore and optimize new chemical synthesis methods to obtain more suitable A-site monovalent ion doping effects.

Herein, in continuation of the hydrothermal synthesis of $La_{1-x-y}Ca_xK_yMnO_3$ (LCKMO) on transport characteristics, we explored the effect of the A-site heterovalent ion doping of LCKMO on its dielectric properties, and the effect of valent ion (K^+) doping on the intrinsic mechanism is elaborated here too. In this study, a series of LCKMO cubic crystals with different contents were successfully synthesized using a hydrothermal method. K^+ doping induces a modification in the coordination environment of Mn. When La^{3+} and K^+ concentrations are simultaneously increased and the Ca^{2+} content is decreased, it induces the presence of multiple valence states of Mn and consequently alters the electron concentration of Mn. More importantly, O exists in an equilibrium-deficient state and therefore does not considerably change for oxygen. This in turn is responsible for the appearance of a negative permittivity of the material. All of these negative permittivity characteristics are successfully achieved in the 20 Hz-2 MHz range.

Results and discussion

An unconventional hydrothermal method was employed to synthesize perovskite manganates with the addition of 60 g of KOH (Scheme 1).[26,27] The large amount of KOH in the hydrothermal autoclave makes the reactant ions to be in a state similar to that of molten salt. The resulting ultra-high-alkaline environment forces K^+ into the LCMO lattice with ease. Moreover, the quasi-melting hydrothermal condition induces the disproportionation reaction of Mn^{4+} and facilitates the doping of three cations (La^{3+}, Ca^{2+} and K^+) into the A site.[28]

Fig. 1a shows the XRD patterns of perovskite $La_{1-x-y}Ca_xK_yMnO_3$ with different La/Ca ratios with the addition of 60 g of KOH. Based on the ratio of La/Ca and K, the samples were named LCKMO-1, LCKMO-2, LCKMO-3, LCKMO-4, LCKMO-5, and LCKMO-6. The XRD patterns of LCKMO are shown in Fig. 1a; after the hydrothermal reaction at 260 °C for 72 h, K^+ gets doped into the lattice and a superlattice is obtained in the range of 5°–20°.[27] In addition, with the increase in the La^{3+} and K^+ concentration in the compound, the diffraction peaks corresponding to the (110)/(104) and (200)/(204) crystal planes of perovskite at 32°–34° and 45°–49° undergo splitting (Fig. 1b and c). The splitting distance increases with the increase in the peak strength of the splitting peak. This is because the radius differences of La^{3+} (0.106 nm), Ca^{2+} (0.099 nm), and K^+ (0.133 nm) in the A-site are considerable. As the La^{3+} and K^+ concentrations increase and the Ca^{2+} concentration decreases, considerable stress is are generated inside the crystal, leading to lattice expansion and results in the splitting of diffraction peaks.[28,29] The increase in peak ratio indicates that the Mn–O–Mn bond angle ($\theta_{Mn-O1}/\theta_{Mn-O2}$) and the Mn–O bond distance (d_{Mn-O}) increases, which indicates that the double exchange interaction between Mn^{3+}–O^{2-}–Mn^{4+} is considerably enhanced and leads to the octahedral distortion of MnO_6,[30–32] thereby

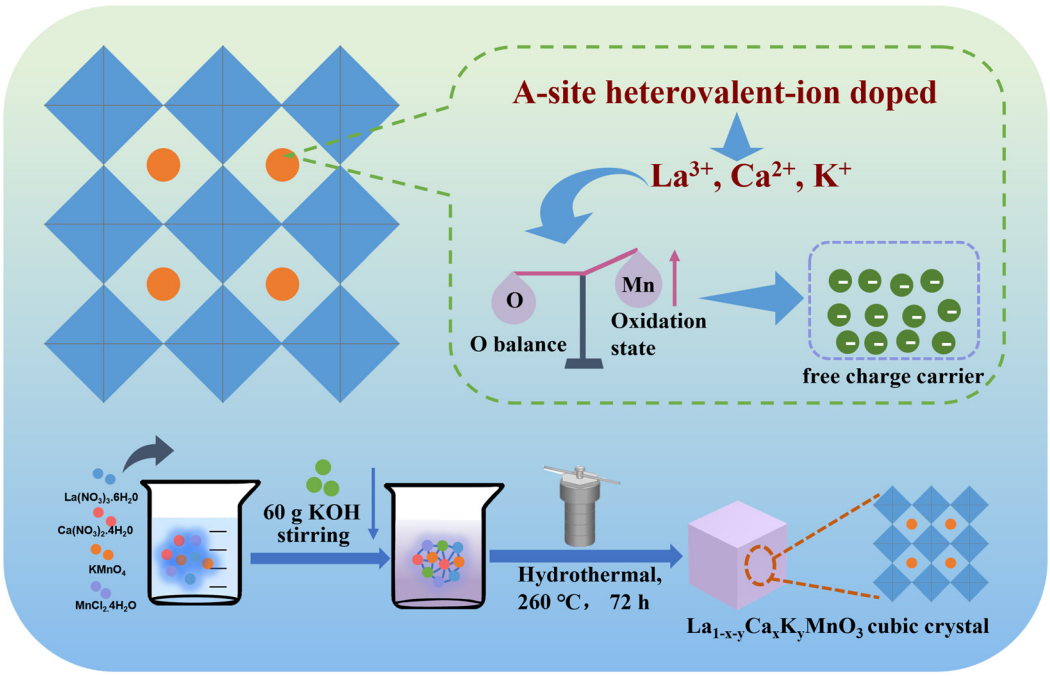

Scheme 1 Schematic of the synthesis route and regulation mechanism of the perovskite LCKMO doped with heterovalent ions.

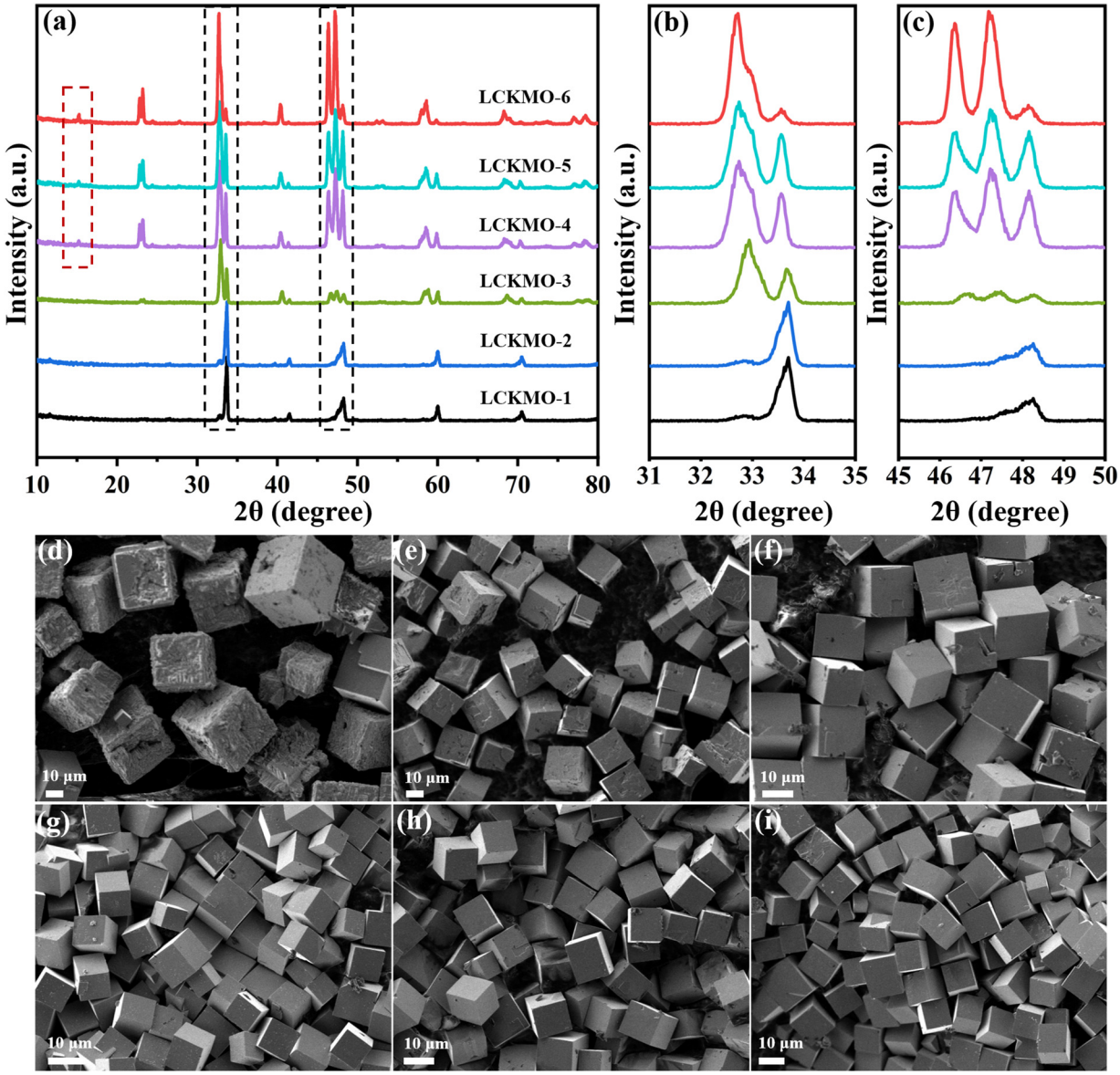

Fig. 1 (a) XRD patterns of $La_{1-x-y}Ca_xK_yMnO_3$ (LCKMO) samples. (b and c). Magnification of the two major diffraction peaks selected. (d–i) SEM images of perovskites LCKMO-1, LCKMO-2, LCKMO-3, LCKMO-4, LCKMO-5, and LCKMO-6.

affecting the crystal structure of LCKMO. As can be seen in Fig. 1d–i, SEM images show that the LCKMO crystals synthesized by the hydrothermal reaction are cubic in shape, with a relatively uniform grain size. The size of cubic crystals is 10–35 μm. Furthermore, the surface of cubic crystal gradually becomes smooth and is compact with a decrease in Ca^{2+} content and an increase in K^+ content, which indicates that maintaining conditions of ultra-high-alkaline concentration solution in a hydrothermal reaction system is beneficial for the regulation of the morphology and size of complete LCKMO cubic crystals.

Next, inductively coupled plasma (ICP) spectroscopy was performed to analyze the content of La, Ca, K and Mn, and the chemical formulae of these materials were determined (Table S1 and Fig. S1†). The energy-dispersive spectrometry (EDS) mapping images were obtained to analyze the element distribution of the LCKMO (Fig. S2†). EDS images demonstrate that the cubic crystal contains La, Ca, and K. The above results indicate that the successful doping of A-site heterovalent ions of perovskite has been achieved in the hydrothermal reaction of ultra-high-alkaline concentration solution system and perfect cubic crystals were obtained.

To research the relationship between the surface valence state information of the samples, XPS spectra were tested to analyze the valence state of LCKMO. Except for the C element, La, Ca, Mn, and O also exist, as can be seen in the XPS spectra (Fig. S3†); the K element cannot be detected owing to the low content of doped K^+. As can be seen in Fig. 2a, the character-

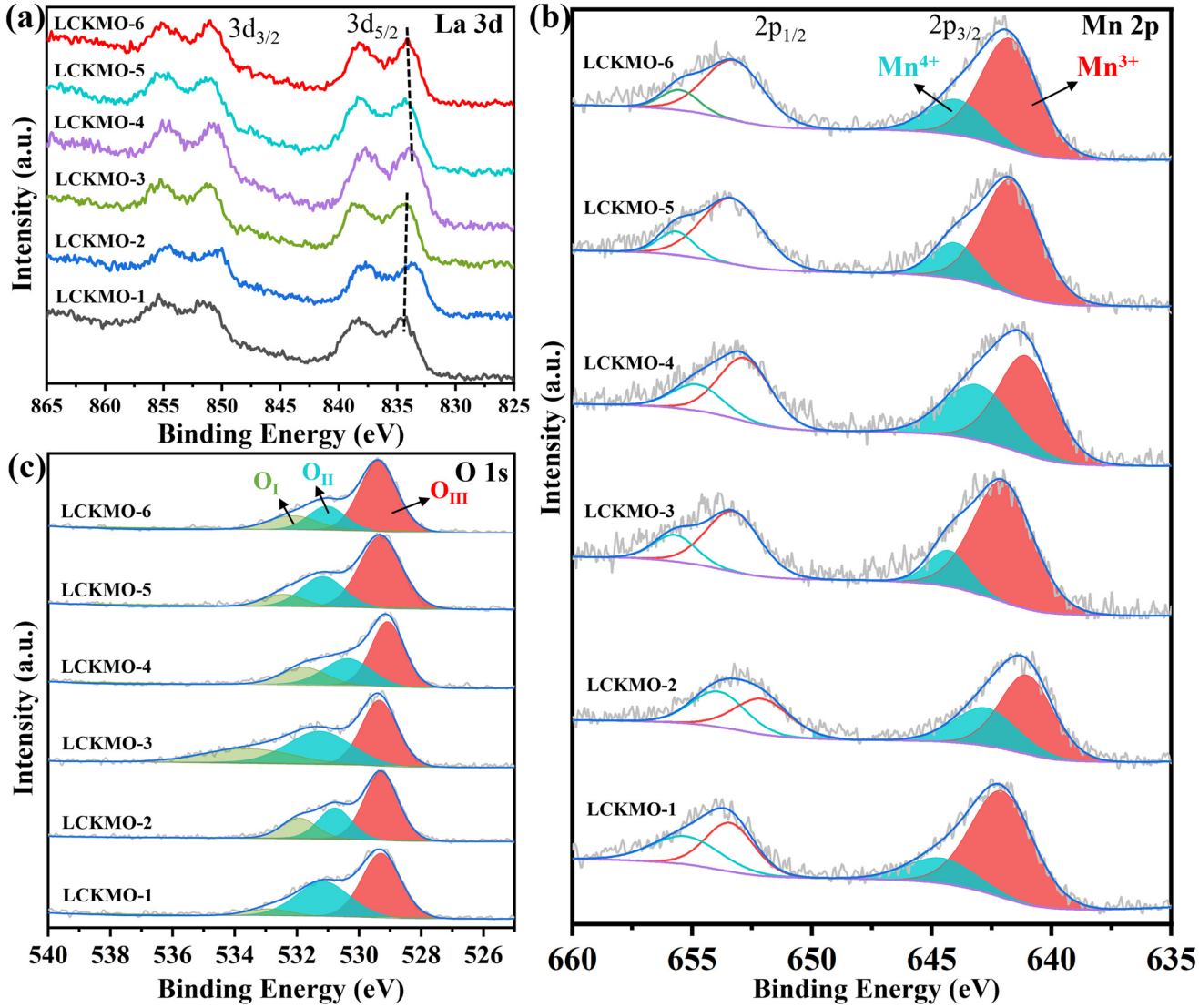

Fig. 2 (a) La 3d XPS spectra, (b) Mn 2p XPS spectra, and (c) O 1s XPS spectra for LCKMO samples.

istic peaks at 852.0 and 835.0 eV are attributed to La $3d_{3/2}$ and La $3d_{5/2}$, respectively.[33,34] Electron transfer from the ligand atom to the ionized $4f_0$ orbital of the La core atom is considered to be the origin of the observed complex peak structure, and the characteristic peak at ~835.0 eV can be related to the electron transfer to the $4f_0$ orbital.[35] In addition, with the increase in concentration of La^{3+} and K^+, the characteristic peak has a slight shift toward a higher binding energy, which indicates the presence of La species with a high oxidation state. As per the Mn 2p XPS spectra shown in Fig. 2b, the characteristic peaks at 654.0 and 642.0 eV are attributed to Mn $2p_{1/2}$ and Mn $2p_{3/2}$, respectively;[36] moreover, the peaks at 542.2 eV and 654 eV are associated with Mn^{3+} species, and peaks at 544.8 eV and 657.8 eV are associated with Mn^{4+} species.[37,38] The peaks of Mn 3d and 2p in LCKMO shift to a high binding energy as the K^+ doping concentration increases, which indicates that high-concentration KOH doping in the hydrothermal reaction system allows Mn species to exist in higher oxidation states and affects the degree of charge order of Mn. As shown in Fig. 2c, in the O 1s XPS spectra, the peaks at 532.1, 531.0 and 529.4 eV belong to O_I (surface adsorbed water), O_{II} (surface adsorbed oxygen) and O_{III} (lattice oxygen), respectively.[39] Table S2† shows the variation of peak area for various oxygen species; from the fitting results of the O 1s peak area, it can be observed that there is little difference in the lattice oxygen content and oxygen defect concentration of a series of LCKMO samples, illustrating that the doping of KOH has a relatively small effect on the valence state change of oxygen. Reports have shown that it is conducive to tune the negative dielectric properties of the sample at different temperatures.[40]

Moreover, to research the effect of doping of A-site heterovalent ions in perovskite LCKMO under ultra-high-alkaline concentration solution on their internal atomic coordination environment, the Mn L-edge, K-edge and O K-edge of the

samples were tested to research their spin states, bond covalent characteristics, and electron density on the outer surface.[41] The peak intensity and peak movement in the XANES spectra represent the orbital occupation state of the atoms.[42] Mn L-edge XAS spectra in Fig. 3a show that peaks at L_3 edge and L_2 edge of LCKMO shift to high energy, which indicates the presence of high oxidation states. The variation of the Mn L-edge indicates that the doping of multiple heterovalent ions in the A-site of LCKMO not only affects the A-site but also changes the coordination environment of Mn. Moreover, in the O K-edge shown in Fig. 3b, peaks A and B belong to Mn 3d and O 2p orbits, respectively, and peak C belongs to the hybridization of A site and O 2p orbits, and peak D belongs to the hybridization of Mn 4sp and O 2p orbits.[42] The peak A and peak B changes are not significant. This result provides a new phenomenon and perspective for the explanation of the mechanism of negative permittivity as it indicates that the advantage of hydrothermal disproportionation provides favorable conditions for the doping of divalent ions in ultra-high-alkaline concentration solutions and balances the coordination environment of O. Therefore, LCKMO may contain various Mn ions (such as La^{3+}, Ca^{2+}, and K^{+}) in different chemical environments, stabilized by adjusting the hybrid orbitals between Mn 3d and O 2p.[43] Subsequently, from the Mn K-edge EXAFS spectra displayed in Fig. 3c, it can be observed that the peak shifts to higher binding energy compared with other samples. To elucidate the local structure of the Mn atom in the perovskite, the K-space and R-space Fourier transform of the EXAFS spectra for Mn K-edge were obtained. As shown in Fig. 3d, in the Fourier-transformed spectra of R-space in LCKMO, peaks at 1.5 Å and 3.5 Å belong to the Mn–O bond and Mn–La/Ca/K coordination bond (without phase correction), respectively.[27,44] The M–O bond of LCKMO-1 has the highest and longest coordination bond intensity, and the M–O bond of LCKMO-6 has the lowest coordination bond intensity. Note that the Mn–La/Ca/K coordination bond intensity of LCKMO-1 is low and slightly shifted to the left, and the Mn–La/Ca/K coordination bond intensity of LCKMO-6 is the largest and the Mn–La/Ca/K bond is the longest. The EXAFS wavelet transform spectra of Mn in Fig. 3e–j shows that the peak positions of K-space and R-space for the Mn–O coordination bond and the Mn–La/Ca/K coordination bond of the sample do not considerably change. However, as the La/Ca and K^{+} concentrations increase, Mn–La/Ca/K coordination bond intensity gradually increases, and the coordination of the covalent bond with O weakens.[45] These results demonstrate that the hydrothermal synthesis method is advantageous for doping divalent metal ions in ultra-high-alkaline concentration solution systems. It can regulate the coordination environment of elements at the A and B sites, resulting in a higher mixed valence state of Mn at the site, which can increase the concentration of free carriers. Moreover, the change in O is not significant. Therefore, based on these changes, we will continue to explore the impact on conductive ability and dielectric properties.

Conductivity, as a key physical quantity characterizing the conductivity characteristics of materials, can effectively reveal the internal carrier transport mechanism of materials. As shown in Fig. 4a, the DC conductivity (σ_{dc}) of the LCKMO system exhibits temperature dependence. Note that as the temperature increases, the conductivity of the 5 sample groups shows a gradually increasing trend. The conductivity of the LCKMO-6 sample first increases and then slowly decreases with temperature changes. The above conductive behaviour can be fitted using the Arrhenius equation:[46]

$$\sigma = Ae^{-E_a/K_B T} \quad (1)$$

where σ is the direct current (DC) conductivity, A is the pre-exponential factor, E_a is the activation energy for conductivity, K_B is the Boltzmann constant, and T is the absolute temperature (K). According to the linear fitting results of the Arrhenius equation (eqn (1)), the activation energies E_a of the LCKMO-1–LCKMO-5 sample groups exhibit low characteristic values, which can be attributed to the conduction mechanism of thermally excited charge carriers in intrinsic semiconductors. However, the LCKMO-6 sample exhibits a unique conductivity behaviour, with its DC conductivity showing a nonmonotonic characteristic of increasing first and then decreasing with the change of temperature. This complex temperature dependence typically indicates the competition or transformation of multiple conduction mechanisms within the material.[47–49] By fitting and analysing the low-temperature region (T < 125 °C) and high-temperature region (T > 125 °C) of LCKMO-6 from eqn (1), the transition temperature is determined to be 125 °C. The transformation of this conductivity behaviour may be attributed to the doping of K^{+}, which generates a large number of free electrons.[50,51] Based on the above experimental results, the conductivity behaviour of the LCKMO system exhibits a plasma characteristic behaviour similar to metals, thus providing the possibility for achieving negative permittivity.[52]

Fig. 4b, c and Fig. S4† show the AC conductivity spectra of LCKMO samples measured at room temperature and various temperatures. As demonstrated in Fig. 4b, K^{+} doping considerably influences the conductivity variation, with the conductivity exhibiting a gradual enhancement as the K^{+} doping concentration increases. Notably, samples containing lower Ca^{2+} and higher K^{+} concentrations display a characteristic decrease in conductivity with increasing frequency, which persists even at high-frequency ranges. This frequency-dependent behaviour of conductivity in metallic materials can be described by the following relationship:[53]

$$\sigma_{ac} = \frac{\sigma_{dc}\omega_\tau{}^2}{\omega^2 + \omega_\tau{}^2} \quad (2)$$

In eqn (2), σ_{dc} is the DC limit of the Drude model, ω_τ is the reciprocal of the collision frequency and relaxation time ($\omega_\tau = 1/\tau$), and ω_τ is the damping parameter. The experimental data shown in Fig. 4b exhibits agreement with the theoretical equation, suggesting that σ_{ac} is predominantly governed by a substantial population of free electrons. Note that the temperature plays a crucial role in determining the electronic states, particularly influencing both electron concentration and mobi-

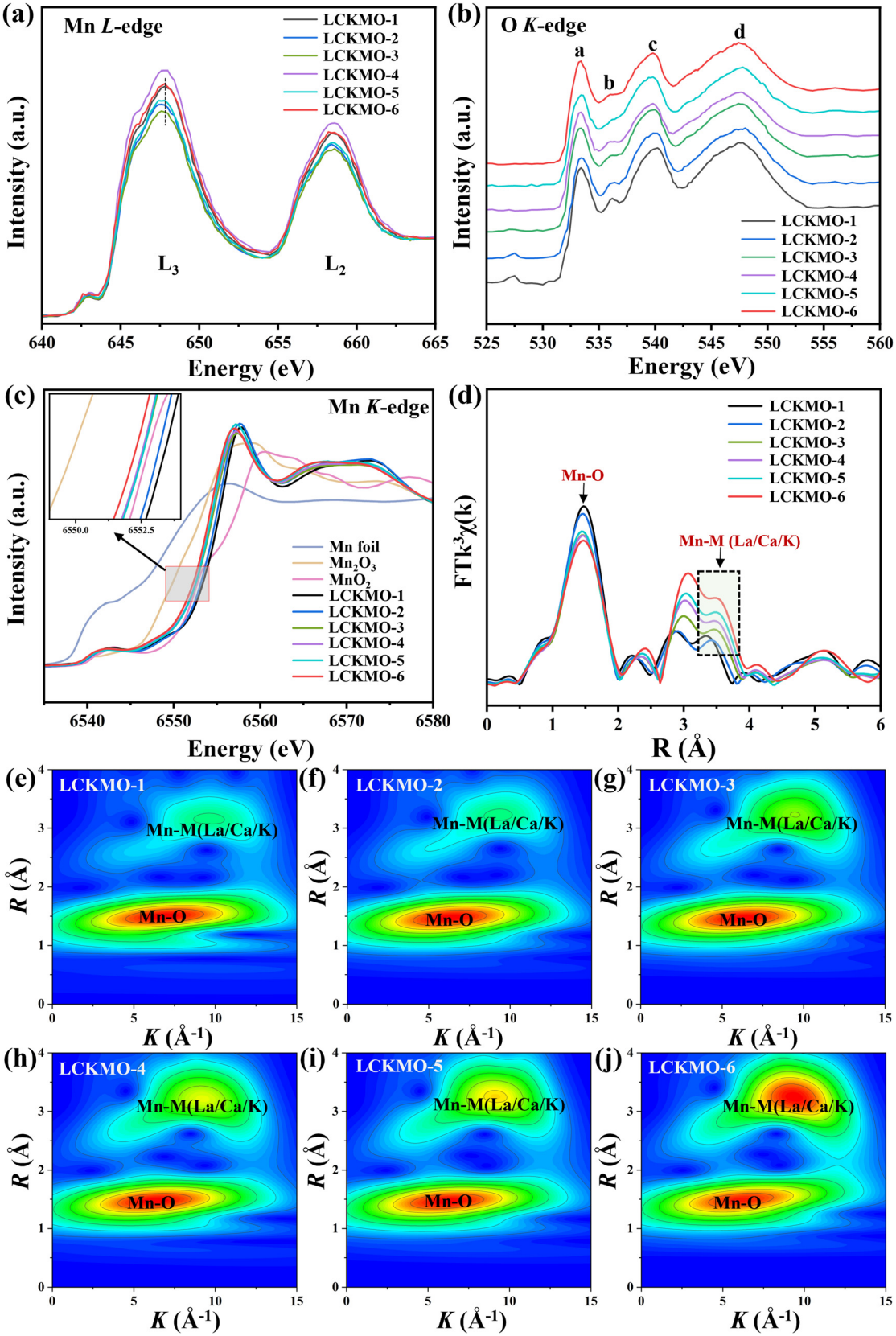

Fig. 3 (a) Mn L-edge X-ray absorption spectra of the perovskite LCKMO. (b) O K-edge X-ray absorption spectra of the perovskite LCKMO. (c) Mn K-edge EXAFS of all perovskite samples. (d) R-space Fourier-transformed FT ($k^3\chi(k)$) of Mn K-edge EXAFS for all perovskite samples. (e–j) Wavelet transforms for the k^3-weighted EXAFS signals for all perovskite samples.

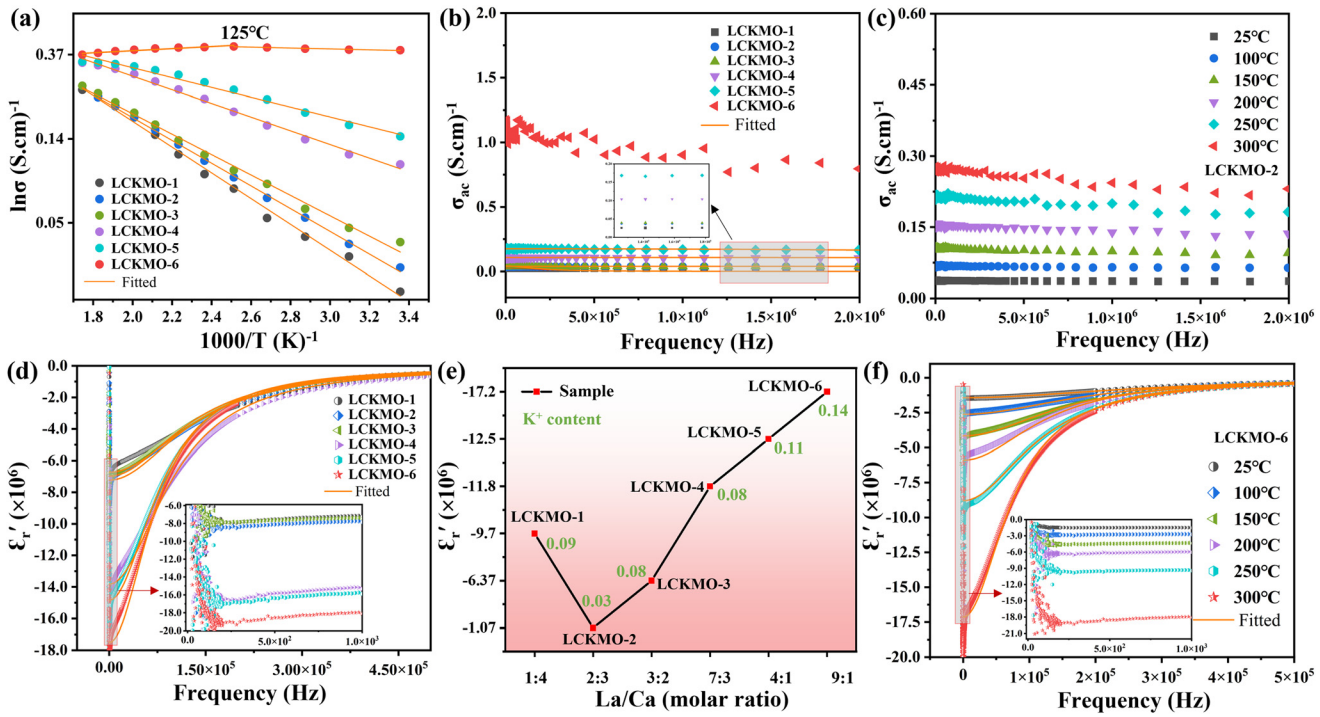

Fig. 4 (a) Temperature-dependent DC conductivity of the perovskite LCKMO. (b) AC conductivity of the perovskite LCKMO at room temperature. (c) AC conductivity of LCKMO-2 as a function of frequency at various temperatures. (d) Negative permittivity of the perovskite LCKMO as a function of frequency at room temperature. (e) Relationship between the extreme value of the negative permittivity and the La/Ca content and the K^+ content. (f) Negative permittivity of LCKMO-6 as a function of frequency at various temperatures. (The orange solid lines in (d) and (f) are the fitting results based on the Drude model. The inset in (b) is the selectively enlarged details in the high-frequency region. The insets in (d) and (f) are the selectively enlarged details in the low-frequency region.).

lity. As demonstrated by Fig. 4c and Fig. S4,† the sample's conductivity demonstrates a remarkable increase with increase in temperature. This phenomenon can be attributed to pronounced phonon scattering effects, where weakly bound electrons gain sufficient energy to overcome ionic potential barriers, thereby increasing the population of unbound electrons;[8] even at high temperatures, it maintains a metallic-like behaviour.

Subsequently, the permittivity (ε_r') and dielectric loss ($\tan\delta$) of perovskite LCKMO as a function of frequency at various temperatures were tested. As can be seen in Fig. 4d, at room temperature, all six sample groups exhibited negative permittivity across the entire experimental frequency range. In the magnified image, it can be seen that the absolute value of the negative permittivity increases with frequency at low frequencies ($<10^3$ Hz). Note that negative permittivity shows a tendency to stabilize at higher frequencies. The relationship between the negative permittivity and the La/Ca content *versus* the K^+ molar ratio provides additional insight into this phenomenon. As can be seen in Fig. 4e, the absolute value of the negative permittivity shows a significant enhancement with increasing K^+ concentration as the La/Ca ratio gradually increases. When the negative permittivity has a negative value throughout the entire measurement frequency range, its absolute value demonstrates a characteristic decrease with frequency similar to the plasma behaviour observed in metallic systems. This similarity arises from the collective oscillation of electrons under external electric field excitation, leading to the induction of a plasma state.[54] From a theoretical perspective, the observed negative permittivity can be attributed to the plasmon of free electrons within the material system. This behaviour is well-described by the Drude model derived from free electron theory, which successfully explains the frequency-dependent variation of the negative permittivity.[49]

$$\varepsilon_r' = 1 - \frac{\omega_p{}^2}{\omega^2 + \omega_\tau{}^2} \quad (3)$$

$$\omega_p = \sqrt{\frac{ne^2}{m^* \varepsilon_0}} \quad (4)$$

In the formula, ω is the angular frequency ($\omega = 2\pi f$), ω_p is the plasma frequency, ne is the effective concentration of free electrons and m^* is the effective mass of electrons, ε_0 is vacuum permittivity (8.85×10^{-12} F m^{-1}). The Drude model (the orange solid lines in Fig. 4d, f and Fig. S5†) agrees well with the experimental results. In addition, as shown in Fig. 4f and Fig. S5,† the negative permittivity of perovskite LCKMO can be observed to vary with the function of frequency at various temperatures. Within the testing range of 20 Hz–

2 MHz, the permittivity remains negative. The absolute value of the negative permittivity increases with the increase in temperature. We this amplified the low-frequency range (<10^3 Hz) of the curve. It can be seen that the negative permittivity of the sample remains almost unchanged with frequency in the low-frequency range. However, as the concentration of K^+ increases, the absolute value of the negative permittivity increases. Thus, the negative permittivity of the same sample increases with temperature, and the absolute value of the negative permittivity at low frequencies also increases. Compared with room temperature, although high temperature increases Drude damping, in simple metal materials, ω_τ is usually considerably lower than ω_P;[55] it is a stable negative value, which indicates that the plasma state will not be destroyed at high temperatures. In addition, it was found that the negative dielectric behaviour at very low frequencies (<10^3 Hz) is not satisfactory. We believe that in the <10^3 Hz range, it can be combined with the previous DC conductivity data to obtain the higher the DC conductivity at low frequencies, the greater the absolute value of the permittivity. This is attributed to the increase in the concentration of free charge carriers. However, the dielectric loss of the sample gradually decreases with frequency. At different temperatures, as the temperature of the sample increases, the dielectric loss shows a decreasing trend (Fig. S6†). This can be attributed to the fact that the higher the temperature, the more intense the electron motion, and dielectric loss may be the main mechanism of conduction loss. Moreover, within the testing range, the dielectric loss of the sample is positive. Under the condition of gradually increasing La/Ca, the dielectric loss decreases as K^+ concentration increases. Compared with other samples, LCKMO-6 has the lowest negative dielectric loss (Fig. S6f†). When K^+ is doped into LCMO, there will be a large number of free electrons in the sample. The increase in carrier concentration and the decrease in resistivity result in the generation of more conduction current, leading to an increase in conduction loss and ε_r' will rapidly decrease at low frequencies. The imaginary part of the permittivity is almost inversely proportional to frequency. This indicates that conduction loss plays a major role.[49] At the high-frequency region, the value of dielectric loss tends to flatten, indicating that polarization loss is dominant.[56] The above results show that doping of various heterovalent ions in the A-site increases the more Mn mixed valence and balances the defective changes in O, which makes the concentration of free carriers reduce, facilitating the optimization of the negative permittivity and the reduction of the dielectric loss.

In addition, we researched the effects of different frequencies on the negative permittivity and dielectric loss of materials within a certain temperature range. As shown in Fig. 5 and Fig. S7,† perovskite LCKMO has an ideal temperature stable negative permittivity constant and low dielectric loss in the range of 25 °C to 300 °C. Furthermore, LCKMO-1, LCKMO-2, LCKMO-3, LCKMO-4, and LCKMO-5 show dielectric relaxation in the range of 200 kHz. To summarize, with the increase in frequency, its permittivity gradually increases and remains below zero. However, when LCKMO-5 is in the range of 200 kHz-2 MHz, the curve gradually tends to flatten and does not change with temperature. The temperature-stable negative permittivity is attributed to the collision frequency

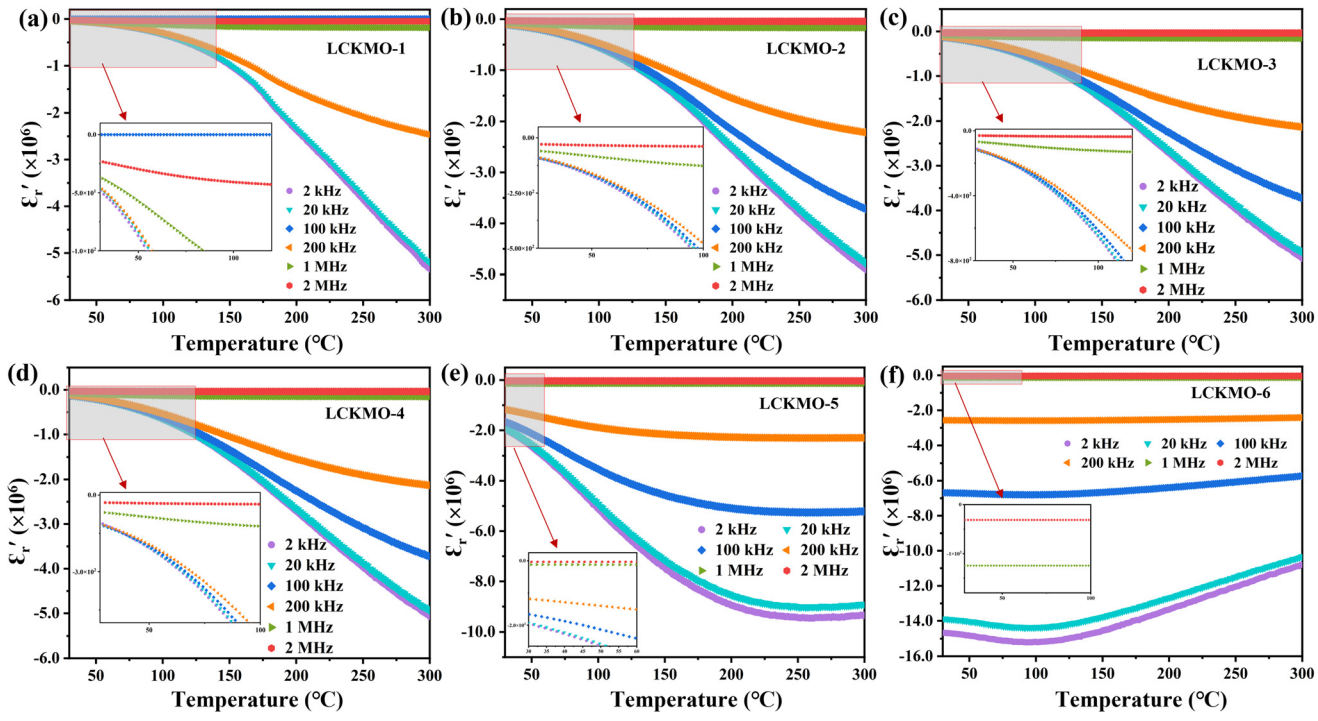

Fig. 5 (a–f) Temperature-dependent negative permittivity (ε_r') of the perovskite LCKMO samples.

(ω_τ) being considerably lower than the plasma frequency (ω_P).[57] The curve of LCKMO-6 in the range of 2 kHz–100 kHz decreases first and then increases, which is different from other samples. Note that their negative permittivity at low frequency reaches 10^6 orders of magnitude; the negative permittivity gradually improves with the increase in frequency, which is consistent with the above phenomenon that the negative permittivity increases as the frequency at temperature change increases. Moreover, their dielectric loss decreases as frequency increases (Fig. S7†). Based on the above results, it can be seen that as La/Ca and K^+ concentrations increase, dielectric loss gradually decreases. In general, with the increase in K^+ doping concentrations, the smaller the negative permittivity, the smaller the dielectric loss. The reason is that in a hydrothermal environment, high-temperature and high-alkali conditions successfully doped heterovalent ions into LCKMO. Therefore, by regulating the A-site metal cation content and changing the mixed valence state of Mn atom in B-site, the generation of free charge carrier is promoted and is beneficial for optimizing its dielectric performance and reducing dielectric losses. Based on the analysis of the above experimental results, it can be concluded that (1) with the increase in K^+ concentration, the absolute value of its negative permittivity is greater, and the dielectric loss is smaller, and (2) the curve change process of the atlas may be closely related to the existence of diodes and superconductors. This study not only makes a significant contribution to the in-depth interpretation of the negative dielectric properties and internal mechanisms of perovskites but also the possibility of diode superconducting phase transition appearing for the first time in an LCKMO cubic crystal.

Conclusion

In summary, we adopted a strategy of doping with heterovalent ions and successfully achieved the doping of A-site divalent ions (La^{3+}, Ca^{2+}, and K^+) in LCKMO through hydrothermal disproportionated reaction at ultra-high-alkaline concentrations. Under these conditions, this doping strategy obtains perfect cubic crystals, changes the proportion of A-site ions, increases the mixed valence state of Mn, enhances the coordination charge density of Mn between the A-site metal cations and balances the coordination environment of oxygen atoms, which increases the concentration of free carriers. By testing the dielectric property, it is found that as the content of K^+ increases, the negative permittivity under variable temperature conditions decreases with increasing temperature. In the variable frequency conditions. Moreover, as the frequency increases, the negative permittivity increases to a value close to zero permittivity, and the dielectric loss decreases to a threshold value close to zero. These results explain that a satisfactory negative permittivity and reduced dielectric losses are obtained. This study not only provides new ideas for the design and optimization of perovskite materials but also provides a new way to regulate the negative permittivity.

Author contributions

Meichun Fu: writing – original draft, investigation, formal analysis, and data curation. Mei Han: review & editing and supervision. Yuan Zhang: resources and survey. Beining Zheng: review & editing, supervision, and investigation. Shouhua Feng: funding acquisition and formal analysis.

Data availability

The authors declare that the data supporting the findings of this study are available within the paper and its ESI files.† Should any raw data files be needed in another format, they are available from the corresponding author upon reasonable request.

Conflicts of interest

There are no conflicts to declare.

Acknowledgements

This work was supported by the Natural Science Foundation of Jilin Province No. 20240101171JC and Experimental Technology Project of Jilin University (SYXM2024a004) and Jilin Science and Technology Development Plan Project (SKL202402007) and the National Key R&D Program of China (2023YFA1506300).

References

1 Z. Leng, Z. Yang, X. Tang, M. Helal, Y. Qu, P. Xie, Z. El-Bahy, S. Meng, M. Ibrahim, C. Yu, H. Algadi, C. Liu and Y. Liu, Progress in percolative composites with negative permittivity for applications in electromagnetic interference shielding and capacitors, *Adv. Compos. Hybrid Mater.*, 2023, **6**(6), 195.
2 X. Zhang, X. Tian, Y. Qin, J. Qiao, F. Pan, N. Wu, C. Wang, S. Zhao, W. Liu, J. Cui, Z. Qian, M. Zhao, J. Liu and Z. Zeng, Conductive metal-organic frameworks with tunable dielectric properties for boosting electromagnetic wave absorption, *ACS Nano*, 2023, **17**(13), 12510–12518.
3 G. Fan, X. Zhang, Q. Wang, R. Su, Y. Tang, C. Hao and Y. Liu, Dielectric evolution of permittivity transition from positive to negative induced by percolation in ceramic composites, *Ceram. Int.*, 2023, **49**(22), 35518–35523.
4 K. Sun, J. Xin, Y. Li, Z. Wang, Q. Hou, X. Li, X. Wu, R. Fan and K. Choy, Negative permittivity derived from inductive characteristic in the percolating Cu/EP metacomposites, *J. Mater. Sci. Technol.*, 2019, **35**(11), 2463–2469.
5 Q. Zhao, J. Zhou, F. Zhang and D. Lippens, Mie resonance-based dielectric metamaterials, *J. Mater.: Today*, 2009, **12**(12), 60–69.

6 H. Gu, J. Guo, Q. He, Y. Jiang, Y. Huang, N. Haldolaarachige, Z. Luo, D. Young, S. Wei and Z. Guo, Magnetoresistive polyaniline/multi-walled carbon nanotube nanocomposites with negative permittivity, *J. Nanoscale*, 2014, **6**(1), 181–189.
7 X. Yao, X. Kou and J. Qiu, Multi-walled carbon nanotubes/polyaniline composites with negative permittivity and negative permeability, *Carbon*, 2016, **107**, 261–267.
8 Z. Wei, Z. Wang, C. Xu, G. Fan, X. Song, Y. Liu and R. Fan, Defect-induced insulator-metal transition and negative permittivity in $La_{1-x}Ba_xCoO_3$ perovskite structure, *J. Mater. Sci. Technol.*, 2022, **112**, 77–84.
9 X. Li, Z. Qian, G. Han, B. Sun, P. Zuo, C. Du, Y. Ma, H. Huo, S. Lou and G. Yin, Perovskite $LaCo_xMn_{1-x}O_{3-\sigma}$ with tunable defect and surface structures as cathode catalysts for Li-O_2 batteries, *ACS Appl. Mater. Interfaces*, 2020, **12**, 10452–10460.
10 T. Tanka, A. Bodhaye, Y. Mukovskii and S. Sanyal, Crystallographic direction dependence of electrical-transport, magneto-transport, magnetic and thermal properties of $La_{0.7}Ca_{0.3}MnO_3$ single crystal, *Mater. Res. Bull.*, 2016, **83**, 250–258.
11 Z. Wang, K. Sun, P. Xie, R. Fan, Y. Liu, Q. Gu and J. Wang, Low-loss and temperature-stable negative permittivity in $La_{0.5}Sr_{0.5}MnO_3$ ceramics, *J. Eur. Ceram. Soc.*, 2020, **40**(5), 1917–1921.
12 M. Arshad, M. Abushad, S. Husain and W. Khan, Investigation of structural, optical and electrical transport properties of yttrium doped $La_{0.7}Ca_{0.3}MnO_3$ perovskites, *Electron. Mater. Lett.*, 2020, **16**, 321–331.
13 S. Suresh, P. Vindhya and V. Kavitha, A comprehensive study of dielectric, magnetic and anticancerous properties of lanthanum manganite perovskite nanoparticles, *J. Alloys Compd.*, 2024, **976**, 173222.
14 P. Rout, S. Pradhan and B. Roul, Dopant mediated multiferroic behavior of $HoMn_{1-x}Co_xO_3$ (x=0, 0.025, 0.05, 0.1), *Ceram. Interfaces*, 2014, **40**, 9647–9655.
15 C. Qian, R. Zhu, H. Li, M. Qin, M. Li, W. Zhang and M. Zhang, Effects of Ba doping on the structural, magnetic and microwave absorption properties for $LaMnO_3$ perovskites, *J. Mater. Sci.: Mater. Electron.*, 2024, **35**, 1395.
16 S. Feng, Y. Zhang, H. Hou, C. Wen, X. Dong, W. Shi, R. Lv, M. Fu, J. Liu, J. Lu, L. Duan, M. Han, B. Zheng and L. Gao, A review of synthesis and novel transport properties of multivalent manganate perovskite: progress, opportunities, and challenges, *Adv. Electron. Mater.*, 2024, **10**, 2300867.
17 X. Xiao, Y. Chu, C. Zhang, Z. Zhang, Z. Qiu, C. Qiu, H. Wang, A. Mei, Y. Rong, G. Xu, Y. Hu and H. Han, Enhanced perovskite electronic properties via A-site cation engineering, *Fundam. Res.*, 2021, **1**, 385–392.
18 Y. Hou, Y. Yao, G. Zhang, Q. Yu and X. Li, Giant dielectric response with an electric field in charge-ordered $La_{1-x}Ca_xMnO_3$ compounds, *J. Am. Ceram. Soc.*, 2009, **92**(6), 1366–1369.
19 K. Sun, P. Yang, Q. He, R. Fan, Z. Wang, J. Tian, X. Yang, W. Duan, X. Wu and Z. Wang, Synergistic effect of dielectric resonance and plasma oscillation on negative permittivity behavior in $La_{1-x}Sr_xMnO_3$ single-phase ceramic, *Ceram. Int.*, 2022, **48**, 8417–8422.
20 K. Yan, L. Shen, F. Yin, G. Qi, X. Zhang, R. Fan and N. Bao, Metallic ferromagnet of $La_{0.5}Sr_{0.5}MnO_3$ with negative permittivity and permeability, *Adv. Electron. Mater.*, 2022, **8**, 2101020.
21 S. Anirban, R. Roy and A. Dutta, Structure, charge carrier conduction, dielectric properties and leakage current density of Dy_2CoMnO_6 double perovskite, *J. Alloys Compd.*, 2022, **928**, 167184.
22 V. Deshmukh, D. Tejashwini, H. Nagaswarupa, R. Naik, A. Al-Kahtani and Y. Kumar, Sr and Fe substituted $LaCoO_3$ nano perovskites: electrochemical energy storage and sensing applications, *J. Energy Storage*, 2024, **89**, 111724.
23 D. Varshney and M. Shaikha, Substitutional effects on structural and magnetotransport properties. of $La_{0.85-x}Sm_xK_{0.15}MnO_3$ (x = 0.05, 0.1 and 0.15), *J. Alloys Compd.*, 2024, **589**, 558–556.
24 D. Kubicki, D. Prochowicz, A. Hofstetter, S. Zakeeruddin, M. Grätzel and L. Emsley, Phase segregation in potassium-doped lead halide perovskites from ^{39}K solid-state NMR at 21.1 T, *J. Am. Chem. Soc.*, 2018, **140**, 7232–7238.
25 H. Cheng, Y. Wang, Y. Jin, B. Zhou, D. Li, S. Mo, X. Liu, W. Si and J. Li, Oxygen vacancy engineering through equivalent and aliovalent doping on $LaCoO_3$, *Sep. Purif. Technol.*, 2024, **351**, 128078.
26 X. Wang, K. Huang, X. Wu, L. Yuan, L. Li, G. Li and S. Feng, Manipulation and observation of atomic-scale superlattices in perovskite manganite, *Chin. Chem. Lett.*, 2023, **34**, 108267.
27 S. Feng, H. Yuan, Z. Shi, Y. Chen, Y. Wang, K. Huang, C. Hou, J. Li, G. Pang and Y. Hou, Three oxidation states and atomic-scale p-n junctions in manganese perovskite oxide from hydrothermal systems, *J. Mater. Sci.*, 2008, **43**, 2131–2137.
28 Y. Zhang, Y. Sun, C. Liu, J. Liu, J. Lu, B. Wang, L. Duan, G. Chen, B. Zheng, M. Han and S. Feng, Pivotal role of modifiable A-site doping in enhancing valence stability and excited state dynamics of MnO_6, *Small Methods*, 2024, 2400539.
29 C. Gao, S. Lin, F. Kun and W. Kui, Effect of oxygen content on the dielectric properties of polycrystalline $BiFeO_\delta$ ceramics, *Acta Phys. Sin. – Ch. Ed.*, 2007, **56**(10), 6068–6074.
30 S. Zhao, X. Yue and X. Liu, Tuning room temperature Tp and MR of $La_{1-y}(Ca_{y-x}\ Sr_x)MnO_3$ polycrystalline ceramics by Sr doping, *Ceram. Int.*, 2017, **43**, 4594–4598.
31 Y. Zhang, X. Tang, Y. Chen, G. Wang and X. Dong, Electrical transport properties in $La_{0.7}Ca_{0.3-x}Sr_xMnO_3$ thin films, *J. Inorg. Mater.*, 2016, **31**, 274–278.
32 D. Cao, Y. Zhang, W. Dong, J. Yang, W. Bai, Y. Chen, G. Wang, X. Dong and X. Tang, Structure, magnetic and transport properties of $La_{0.7}Ca_{0.3-x}Sr_xMnO_3$ thin films by sol–gel method, *Ceram. Int.*, 2015, **41**, S381–S386.
33 M. Sunding, K. Hadidi, S. Diplas, O. Løvvik, T. Norby and A. Gunnæs, XPS characterisation of in situ treated lantha-

num oxide and hydroxide using tailored charge referencing and peak fitting procedures, *J. Electron Spectrosc. Relat. Phenom.*, 2011, **184**, 399–409.
34 H. Wang, M. Zhou, P. Choudhury and H. Luo, Perovskite oxides as bifunctional oxygen electrocatalysts for oxygen evolution/reduction reactions-a mini review, *Appl. Mater. Today*, 2019, **16**, 56–71.
35 C. Jørgensen and H. Berthou, Split photo-electron signals from the unique closed shell cation lanthanum(III), *Chem. Phys. Lett.*, 1972, **13**, 186–189.
36 J. Lasluisa, F. Huerta, D. Amorós and E. Morallon, Carbon material and cobalt-substitution effects in the electrochemical behavior of $LaMnO_3$ for ORR and OER, *Nanomaterials*, 2020, **10**(12), 2394.
37 Y. Zhu, W. Zhou and Z. Shao, Perovskite/carbon composites: applications in oxygen electrocatalysis, *Small*, 2017, **13**, 1603793.
38 H. Zhao, L. Zhu, J. Yin, J. Jin, X. Du, L. Tan, Y. Peng, P. Xi and C. Yan, Stabilizing lattice oxygen through Mn doping in $NiCo_2O_{4-\delta}$ spinel electrocatalysts for efficient and durable acid oxygen evolution, *Angew. Chem., Int. Ed.*, 2024, **63**, e202402171.
39 Y. Guo, S. Wang, R. Li, J. Yu, X. Zhang, M. Li, X. Zheng, J. Zhu, Y. Song, G. Wang and X. Bao, In situ exsolved CoFe alloy nanoparticles for stable anodic methane reforming in solid oxide electrolysis cells, *Joule*, 2024, **8**(7), 2016–2032.
40 X. Chu, K. Huang, C. Hou, L. Ge, X. Wu, Y. Du and S. Feng, Controlled synthesis and properties of $La_{1-x-y}Ca_xK_yMnO_3$, *Chem. J. Chin. Univ.*, 2012, **34**, 40–44.
41 X. Wang, Z. Pan, X. Chu, K. Huang, Y. Cong, R. Cao, R. Sarangi, L. Li, G. Li and S. Feng, Atomic–scale insights into surface lattice oxygen activation at the spinel/perovskite interface of $Co_3O_4/La_{0.3}Sr_{0.7}CoO_3$, *Angew. Chem., Int. Ed.*, 2019, **58**(34), 11720–11725.
42 S. Susarla, P. Fernández, C. Ophus, S. Das, P. Puente, M. McCarter, P. Ercius, L. Martin, R. Ramesh and J. Junquera, Atomic scale crystal field mapping of polar vortices in oxide superlattices, *Nat. Commun.*, 2021, **12**(1), 6273.
43 H. Wu, T. Hu, C. Martin, A. Maignan, J. Cezar, A. Tanaka, N. Brookes, D. Khomskii and L. H. Tjeng, Ising magnetism and ferroelectricity in Ca_3CoMnO_6, *Phys. Rev. Lett.*, 2009, **102**(2), 026404.
44 Y. Shen, Y. Zhu, J. Sunarso, D. Guan, B. Liu, H. Liu, W. Zhou and Z. Shao, New phosphorus–doped perovskite oxide as an oxygen reduction reaction electrocatalyst in an alkaline solution, *Chem. – Eur. J.*, 2018, **24**(27), 6950–6957.
45 X. Wang, X. Li, X. Chu, R. Cao, J. Qian, Y. Cong, K. Huang, J. Wang, C. Redshaw, R. Sarangi, G. Li and S. Feng, Manipulating surface termination of perovskite manganate for oxygen activation, *Adv. Funct. Mater.*, 2021, **31**, 2006439.
46 A. Glaudell, J. Cochran, S. Patel and M. Chabinyc, Impact of the doping method on conductivity and thermopower in semiconducting highly doped electronic polymers, *Adv. Energy Mater.*, 2015, **5**(4), 1401072.
47 B. Kumar, N. Prasad, G. Prasad and G. Kumar, Synthesis, DC conductivity and dielectric studies on double doped strontium bismuth niobate ceramics, *Mater. Today: Proc.*, 2019, **11**, 1036–1040.
48 R. Nassera, W. Othmena and H. Elhouichetb, Effect of Sb doping on the electrical and dielectric properties of ZnO nanocrystals, *Ceram. Int.*, 2019, **45**, 8000–8007.
49 G. Fan, Z. Wang, K. Sun, Y. Liu and R. Fan, Doped ceramics of indium oxides for negative permittivity materials in MHz-kHz frequency regions, *J. Mater. Sci. Technol.*, 2021, **61**, 125–131.
50 A. Stewart, A. Julien, D. Regaldo, P. Schulz, B. Soucase, D. Ceratti and P. López-Varo, Shedding light on electronically doped perovskites, *Mater. Today Chem.*, 2023, **29**, 101380.
51 D. Federico and C. Ciracì, Impact of surface charge depletion on the free electron nonlinear response of heavily doped semiconductors, *Phys. Rev. Lett.*, 2022, **129**, 123902.
52 V. Prigodin and A. Epstein, Nature of insulator-metal transition and novel mechanism of charge transport in the metallic state of highly doped electronic polymers, *Synth. Methods*, 2001, **125**(1), 43–53.
53 Z. Wang, K. Sun, P. Xie, Y. Liu, Q. Gu and R. Fan, Permittivity transition from positive to negative in acrylic polyurethane-aluminum composites, *Compos. Sci. Technol.*, 2020, **188**, 107969.
54 C. Cheng, R. Fan, Z. Wang, Q. Shao, X. Guo, P. Xie, Y. Yin, Y. Zhang and Y. Lei, Tunable and weakly negative permittivity in carbon/silicon nitride composites with different carbonizing temperatures, *Carbon*, 2017, **125**, 103–112.
55 J. Pendry, A. Holden, W. Stewart and I. Youngs, Extremely low frequency plasmons in metallic mesostructures, *Phys. Rev. Lett.*, 1996, 764773–764776.
56 K. Sun, P. Xie, Z. Wang, T. Su, Q. Shao, J. Ryu, X. Zhang, J. Guo, A. Shankar and J. Li, Flexible polydimethylsiloxane/multi-walled carbon nanotubes membranous metacomposites with negative permittivity, *Polymer*, 2017, **125**, 50–57.
57 S. Maier, Electromagnetics of metals, plasmonics: fundamentals and applications, *Nanoplasmonics: Fundam. Appl.*, 2007, 5–19.

